

# Characteristics of GTA fusion zones and heat affected zones in superalloy 713C

M.B. LACHOWICZ\*, W. DUDZIŃSKI

Wroclaw University of Technology, Institute of Materials Science and Applied Mechanics, Wroclaw, Poland

In this paper, metallographic examinations, characterising microstructural changes in the 713C superalloy subjected to remelting by GTA method, are presented. In the fusion zone, precipitation of  $M_{23}C_6$  or  $M_6C$  carbides based on chromium and molybdenum was observed. Eutectic mixtures of  $(\gamma-\gamma')$ - $M_xC_y$  type with highly developed morphology were also perceived. It was found that, in the matrix areas with non-homogeneous chemical composition, the eutectic reaction  $\gamma-\gamma'$  can occur at the temperature close to that of the precipitation of the  $M_xC_y$  carbides. The presence of silicon in the carbide phases can be conducive to lowering their solidification point by creating low-melting compound NbSi. Both in the fusion zone (FZ) and in the heat-affected zone (HAZ), the secondary precipitates of the  $Ni_3(AlTi)-\gamma'$  phase, varying in size from 50 to 100 nm, were found. The lattice mismatch factor of the  $\gamma$  and  $\gamma'$  particles was +0.48 % to +0.71 %, which is characteristic of the coherent precipitates of the  $Ni_3Al$  phase enriched with titanium. No dislocations or stacking faults were observed in the microstructure of the FZ. In the HAZ, some primary undissolved  $\gamma'$  precipitates, with a part of aluminium probably replaced with niobium were observed, which raised their melting point.

Keywords: 713C alloy, heat affected zone,  $Ni_3Al$ , hot crack, lattice mismatch factor

© Wroclaw University of Technology.

## 1. Introduction

Industrial superalloys based on nickel and  $Ni_3Al$  phase demonstrate susceptibility to strain-age cracking as well as to solidification- and liquation-related hot cracking. Weldability and mechanical properties of precipitation-hardened alloys are strongly dependent on the quantity and morphology of the intermetallic phase  $Ni_3Al(Ti)$ . Along with increasing  $\gamma'$  content, related to increasing Ti and Al content above a critical value, the alloys become less weldable [1–6].

In nickel-based superalloys, solidification- and liquation-related cracks are caused by the high content of alloyed elements, dendritic segregation in cast alloys and very wide range of melting temperatures of the alloys and the occurring phases. This leads to the precipitation of the phases arising directly from the liquid, mainly carbides, carbonitrides and borides, as well as developed carbide-based eutectics with  $\gamma-\gamma'$  matrix and low-melting, zirconium-rich eutectics. As a result of the heat

effect, first of all, the  $M_{23}C_6$ ,  $M_6C$  and MC primary carbides precipitated on the grain boundaries which are subject to melting. The complex carbides containing Cr, Mo and Fe are subject to decomposition at relatively low temperatures between 750 and 1050 °C, but the MC-type carbides like NbC, TiC, (NbTi)CN turn into liquid within the temperature range of 1100 to 1200 °C [7–16]. However, the decomposition temperature of MC carbides is strongly dependent on niobium-to-titanium replacement. Chen *et al.* [17–19] also associated the melting of the grain boundaries in the 718 alloy with the segregation of boron towards the grain boundaries. The segregation of boron and formation of niobium carboborides locally decreased the melting point even by *ca.* 200 °C with respect to niobium carbides.

Ojo, Lippold, Huaxin and Liu [20–22] proved that liquation cracks can be caused by low-melting eutectics, rich in zirconium. In the HAZ of welded IC218 alloy, Huaxin identified  $Zr_{15}(Ni,Al,Cr)_{85}$  phases of  $M_5Zr$  type and eutectic mixture Ni- $Ni_5Zr$  with the melting point of 1175 °C [19, 20]. Ojo [22] identified  $Ni_7Zr_2$  and  $Ni_5Zr$  compounds in the

\*E-mail: maciej.lachowicz@pwr.wroc.pl

HAZ of GTA-welded Inconel 738 LC alloy. The zirconium-rich areas were located at the edges of  $\gamma$ - $\gamma'$  eutectics, on the dendrite boundaries of the base material. Ojo noticed three types of possible eutectics with boron, carbides and zirconium, defined by general formulae  $M_3B_2-\gamma$ ,  $Ni_7Zr_2-(\gamma-\gamma')$  and  $MC-(\gamma-\gamma')$ .

Beside the eutectics containing zirconium, carbides and borides, Ojo, Richards and Chaturvedi analysed in detail the formation of the  $\gamma$ - $\gamma'$  type eutectics which is conducive to liquation cracking [22–25]. The authors considered also the possibility of decohesion and melting of the interface between  $\gamma'$  particles and  $\gamma$  solution. This was caused by reaching, on the  $\gamma$ - $\gamma'$  boundary, the aluminium and nickel concentration close to the eutectic composition. According to the authors, the eutectic mixture occurs at the temperature by *ca.* 20 °C lower than the solidification finish temperature, equal to 1198 °C. In the eutectic areas  $\gamma$ - $\gamma'$ , the authors observed voids and shrinkage cavities, caused by the solidification shrinkage. In addition, the decomposition degree of  $\gamma'$  particles depended on the initial size of the particles and the heating rate of the alloy. The authors considered possible transition reactions of  $\gamma'$  particles and suggested that, firstly, the  $\gamma$  phase emerged from the liquid and then, after reaching the eutectic temperature, the  $\gamma$ - $\gamma'$  mixture was formed. When the temperature decreased, the supersaturated  $\gamma$  phase could precipitate from the  $\gamma'$  phase again.

The problem of changes in the decomposition temperature depending on chemical composition, morphology and size of  $\gamma'$  particles in the welded joints is intensively studied as it is the cause of cracking in the alloys based on nickel and  $Ni_3Al$  phase.

## 2. Methodology

The chemical composition of the examined 713C alloy was as follows: Cr 12.8 %, Mo 4.15 %, Nb 1.73 %, Al 6.2 %, Ti 1.04 %, C 0.12 %, B 0.017 %, Zr 5ppm, Fe 0.19 %, Ni – remainder. The alloy was vacuum-cast in a ceramic mould in the form of plates with dimensions of  $120 \times 70 \times 5$  mm. The fusion zones were made in the specimens of  $70 \times 60 \times 5$  mm, obtained from the plates.

The purpose of the research was the simulation of the phenomena which occur in the weld and the HAZ during welding and comparison of the results with the results obtained for the fusions prepared with electron beam, as presented in [26, 27]. The GTA fusion zones were prepared in the Welding Technology Department of Wroclaw University of Technology. The fusions – welds were made at 50 A / 70 V ac. The fusion rate – welding rate was *ca.* 2.5 to 3 mm/s.

Solidification rate of the welds was not tested. However, a temperature change in HAZ during welding was investigated in our previous work [28]. The temperature of 800 °C in HAZ during the welding was obtained after 55 s. During cooling, the temperature in HAZ decreased to 400 °C after 75 seconds and 200 °C after 180 seconds.

Metallographic examination was carried out by light and electron microscopy, using the scanning microscope JEOL JSM-5800LV-Oxford LINK ISIS-300 and transmission microscopes Philips EM301 and EM 400. Polished sections for light and SEM observations were etched with the reagent ML0 and ML3 [26, 27]. The foils for TEM observations were prepared in the plane parallel to the welds. The phase analysis on the basis of electron diffraction patterns was performed using the Dyfr-Pol programme developed by the authors in the Materials Science Group of Wroclaw University of Technology.

## 3. Macrostructure observations

In the final area of the fusion zone, at *ca.* 2 cm from the terminal crater, an extensive interdendritic microporosity and numerous delaminations parallel to the FZ axis were found. The occurrence of these defects is related to missing weld deposit and volume shrinkage at the final FZ. No cracks were observed in the microporosity area. The morphology of the final FZ area is shown in Fig. 1. In the FZ, only one crack was found, running perpendicularly to the longitudinal axis. The crack is located mainly in the FZ and ends with its one side in the HAZ. Its nature indicates that it is a hot crack caused by solidification stresses. It could propagate in the dendrite boundaries. On the internal edges of the crack,

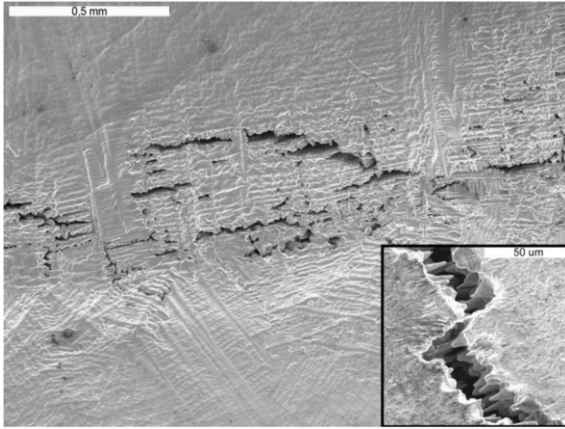


Fig. 1. Dendritic microporosity at the final FZ area. There are visible material delaminations running through the FZ axis. The magnified frame shows the edge of the only crack running perpendicularly to the FZ axis. Visible conical forms are dendrite arms or bridges resulting from material tension during cracking. SEM, SE, 20 kV.

conical forms are observed. They can be dendrite arms, but they can also be recognised as bridges created as a result of the tension during cracking of the material still characterised by sufficiently high plasticity.

### 3.1. Observations of microstructure in the FZ and the HAZ

The microstructure observed on the polished section perpendicular to the FZ axis was mainly characterised by the cellular-dendritic morphology. The structure observed on the longitudinal section – on the FZ face – was also characterised by cellular-dendritic arrangement, however, the cellular arrangement was also locally observed.

The average cell size determined on the longitudinal section was *ca.* 0.05 mm. In the intercellular and interdendritic areas, re-solidified (RS) carbides occurred and a segregation could be observed in the chemical composition as well as in the arrangement and the morphology of the phases in the matrix. In the FZ, the areas with the specific arrangement of dendrites with different crystallographic orientations were observed, similarly as in the FZ made with electron beam, described in [26, 27]. No distinctly outlined grain boundaries were perceived.

Transcrystallisation occurred in the central fusion zone, resulting in lack of discontinuities. The arrangement of dendrites indicated their directional growth.

In the HAZ, the developed precipitates of re-crystallized and undissolved primary carbides were found. This shows slight differences in the chemical composition of primary carbides, that can be caused by different melting point or locally non-homogeneous temperature distribution in the HAZ. No sharp interface was found between the primary and the RS carbides.

In the FZ, some microporosities, occurring mainly in the intercellular and interdendritic areas, were found in the subsurface layer of the weld root.

In the microporosity area, the RS carbides with a characteristic cellular shape could be observed. Such a shape of the carbides results from a discontinuous precipitation from the supersaturated solid solution.

The discontinuous precipitation is caused by an intensive segregation of alloying components and rapid cooling.

The carbides, with the shape similar to the developed carbides  $M_6C$  or  $M_{23}C_6$ , were also found in the intercellular areas. Beside the complex  $M_xC_y$  carbides, the eutectic  $\gamma-\gamma'$  mixtures were also observed. Thus, the complex carbides  $M_xC_y$  can form the developed mixtures of  $M_xC_y-(\gamma-\gamma')$  type. The shrinkage porosities occurring in this area indicate that these can be eutectic mixtures with the melting point below that of the  $\gamma-\gamma'$  matrix.

The occurrence of the eutectics and microporosities in the area adjacent to the FZ root can be explained by higher cooling speed of the FZ root than of the FZ face. The boundary area between the FZ, the HAZ and the base material, as well as the morphology of carbides and microporosity in the FZ root area is shown in Fig. 2.

### 3.2. Identificaton of structure components in the FZ and the HAZ

The presence of agglomerated carbide precipitates was found at the base of the crack, shown in the magnified frame in Fig. 1. The observed precipitates are shown in Fig. 3. Spot chemical microanalysis

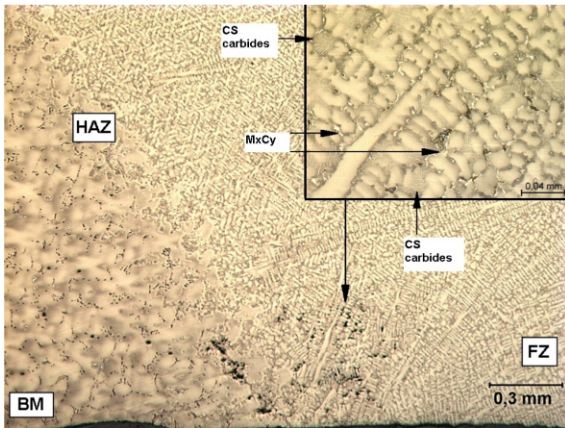


Fig. 2. The microstructure of the base material BM, the FZ and the HAZ as well as visible microporosity in the surroundings of the FZ root. The magnified frame shows microporosity, lamellar carbides created during discontinuous transformation and developed mixtures  $(\gamma-\gamma')-(M_xC_y)$ . Etched with ML3.

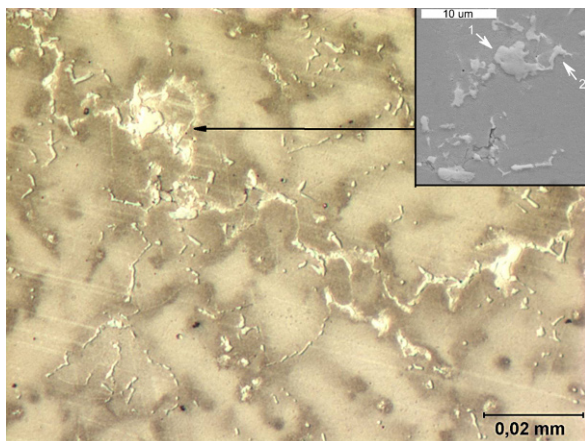


Fig. 3. Combined precipitates of low-melting RS carbides or  $(\gamma-\gamma')-(M_xC_y)$  eutectic mixtures on an extension of a material delamination in the FZ. The magnified picture shows the carbide precipitates, probably  $M_{23}C_6$  or  $M_6C$  type. Etched with ML3. SEM, SE, 20 kV.

of the carbides visible in the locations marked 1 and 2 revealed niobium- and molybdenum-based carbides. The results of microanalysis within the carbides No. 1 and No. 2 are given in Table 1 in weight and atomic percentages.

The values of atomic percentages indicate that the observed area probably includes  $M_{23}C_6$  or  $M_6C$ –

Table 1. The microanalysis within the carbides No. 1 and No. 2 shown in Fig. 3, in weight and atomic percentages.

Point	Ni	Cr	Mo	Ti	Fe	Al	Nb
No. 1 [wt%]	43.02	23.38	28.96	0.95	1.09	2.59	–
No. 1 [at%]	45.24	27.76	18.64	1.23	1.21	5.92	–
No. 2 [wt%]	34.84	14.98	–	6.69	1.42	1.02	41.05
No. 2 [at%]	38.88	18.88	–	9.15	1.67	2.47	28.95

$Cr_3Mo_3C$  type carbides based mainly on chromium, molybdenum and  $(NbTi)C$ . The increased content of nickel, aluminium and chromium suggest that the precipitates are thin and the analysis includes the matrix as well.

The occurrence of the precipitates of that type, characterized by the melting point higher than the  $\gamma-\gamma'$  matrix, indicates that the crack – material delamination could propagate through the liquid phases present on the dendrite boundaries. The decomposition temperature of the  $M_{23}C_6$  and  $M_6C$  carbides is relatively low and ranges from 760 to 1050 °C [7–11]. Thus, it can happen that the matrix is supersaturated by the components coming from the carbides and reaches eutectic composition in these areas.

However, the  $(\gamma-\gamma')$  eutectics were not found in the surroundings of the crack on the polished section shown in Fig. 3. As Ojo demonstrated in [22–25] for Inconel 738, the liquation cracking can be related to the formation of  $(\gamma-\gamma')$  eutectics.

The eutectic mixtures of  $(\gamma-\gamma')-(M_xC_y)$  and  $(\gamma-\gamma')$  as well as  $M_xC_y$  carbides with highly diversified morphology were observed on the face surface of the FZ. However, these inclusions were not accompanied by material discontinuities and microporositities. The FZ face is the last solidifying zone, remaining hot for the longest period of time. So, in contrast to the intercellular areas, it has not nucleated from the liquid alloy. This also shows that in the non-homogeneous areas of the matrix, the  $(\gamma-\gamma')$ -eutectic reaction can occur at the temperature close to the temperature of  $M_xC_y$  carbide precipitation.

According to Ojo [22–25], the  $(\gamma-\gamma')$ -eutectic reaction in 738 Inconel occurs at the temperature of

Table 2. The microanalysis within the carbides No. 1 and No. 2 shown in Fig. 5, in weight and atomic percentages.

Point	Ni	Cr	Mo	Ti	Fe	Al	Nb	Si
No. 1 [wt%]	6.10	3.07	–	17.04	–	–	73.79	–
No. 1 [at%]	7.91	4.49	–	27.10	–	–	60.49	–
No. 2 [wt%]	41.85	17.28	20.49	1.27	1.08	1.02	13.39	3.61
No. 2 [at%]	44.13	20.57	13.22	1.65	1.27	2.34	8.92	7.97

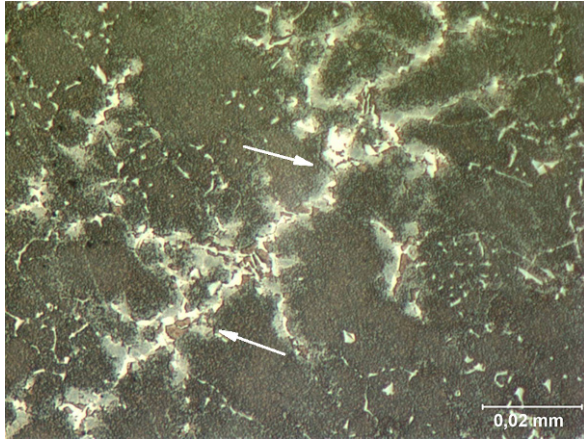


Fig. 4. Developed precipitates of RS carbides or eutectic mixtures on the FZ face surface – indicated by an arrow. Etched with ML3.

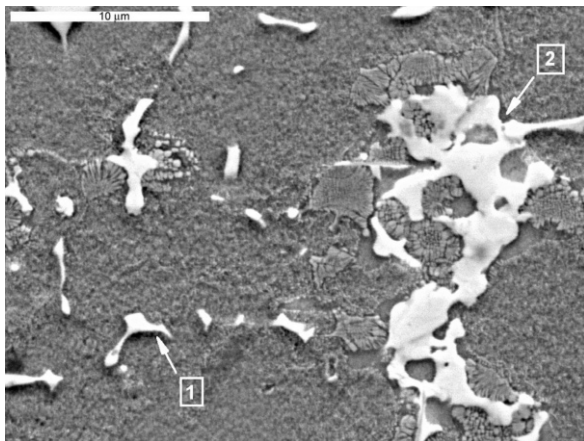


Fig. 5. The magnified  $(\gamma-\gamma')$ - $(M_xC_y)$  eutectic area shown in Fig. 4. Etched with ML3. SEM, SE, 20 kV.

1180 °C or even lower. Therefore, only one eutectic mixture  $(\gamma-\gamma')$ - $M_xC_y$  can occur.

Identification of the so developed eutectic mixture in the FZ confirms that the segregation of alloying elements must be high. The  $\gamma$  matrix and  $\gamma'$

phase are supersaturated with the carbide-forming elements. The example of the observed  $(\gamma-\gamma')$ - $M_xC_y$  eutectic inclusions is shown in Figs. 4 and 5.

The chemical microanalysis of the precipitates shown in Fig. 5 revealed mainly the occurrence of molybdenum, niobium, chromium and silicon. Nickel was also found but, due to the small size and thickness of the precipitates, it could essentially come from the matrix. In the precipitate marked “1” in Fig. 5, mainly niobium and titanium were found, which indicates the occurrence of  $(NbTi)C$  carbide. The phases marked “2” are composite carbides, probably of  $M_{23}C_6$  ( $Cr, Mo, Nb, Si$ ) $_{23}C_6$  type. The results of the microanalysis within the carbides No. 1 and No. 2 are given in Table 2 in weight and atomic percentages.

Silicon can come from impurities, but it also shows a tendency to form a low-melting compound with niobium ( $NbSi$ ). The  $NbC$  and  $NbSi$  compounds can form low-melting eutectics with the  $\gamma$  solid solution. It should be noted that the atomic concentrations of niobium and silicon are similar, but the carbides  $(NbTi)C$  are less stable than  $NbC$  and they show a tendency to decompose into  $M_6C$  and  $M_{23}C_6$  carbides [8, 11, 16]. So, it is highly probable that the analysed precipitate includes a complex eutectic mixture or developed, composite carbide. The presence of the  $(\gamma-\gamma')$ -eutectics indicates rather the occurrence of the  $(\gamma-\gamma')$ - $(M_xC_y)$  eutectic mixture. No zirconium was found in the observed precipitates.

#### 4. Identification of carbides in the FZ using TEM

The microstructure observations using TEM allowed the identification of carbide precipitates in

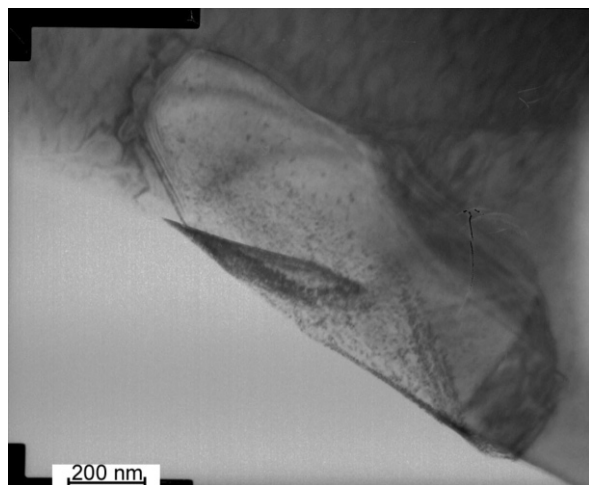


Fig. 6. A (TiNbC)(TiMoC)-type RS carbide in the FZ. TEM, bright field.

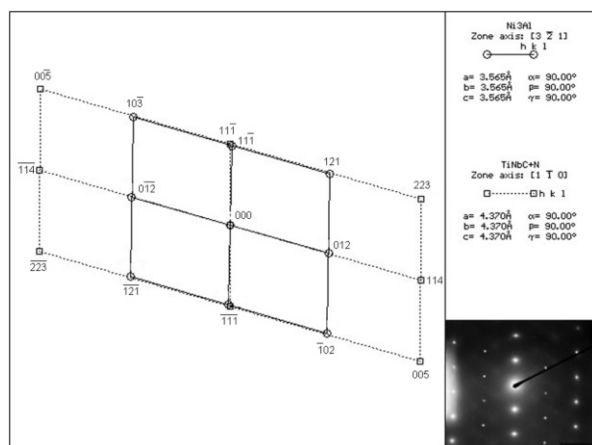
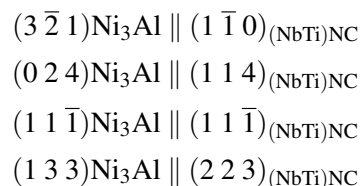


Fig. 7. An example of the electron diffraction pattern and its interpretation for the (NbTi)NC carbide and Ni<sub>3</sub>Al phase shown in Fig. 6.

the FZ. An interpretation of electron diffraction patterns revealed that at least two types of carbides and carbonitrides occur in the FZ: (NbMo)C, (NbTi)NC and M<sub>23</sub>C<sub>6</sub>. The MC type carbides and carbonitrides of niobium, titanium and molybdenum crystallize in the face-centred cubic Fm3m lattice and can also appear in the FZ structure. No dislocations were observed on the carbide-matrix interface.

An example of the MC carbide is shown in Fig. 6 and its typical diffraction pattern with the corresponding description is shown in Fig. 7.

The interpretation of the diffraction patterns proves that for the selected directions and planes, the MC carbides can reveal a coherence with the Ni<sub>3</sub>Al phase and probably also with the  $\gamma$  solid solution. The formation of a coherent boundary requires minimum energy, thus such boundary can be formed during rapid cooling. The lattice of the analysed MC carbides and the interplanar spacing for some planes correspond to the  $\gamma$  and  $\gamma'$  phases which crystallize in the A1, Fm3m and Pm3m lattices [28–36]. The crystallographic relationships of the coherence are as follows:



The precipitates of the M<sub>23</sub>C<sub>6</sub> carbides observed in the FZ are shown in Fig. 8. The interpretation of the electron diffraction patterns indicates their formulae as Cr<sub>23</sub>C<sub>6</sub> and (Cr,Mo)<sub>23</sub>C<sub>6</sub>. The compounds solidify in the face-centred cubic Fm3m lattice. An example of the electron diffraction pattern of the carbide with the corresponding description is shown in Fig. 9. On the diffractogram, some reflections coming from the planes of numerous tiny precipitates of the intermetallic Ni<sub>3</sub>Al phase present in the FZ matrix can be identified.

## 5. Observation of $\gamma'$ phase using SEM and TEM

### 5.1. $\gamma'$ phase in the HAZ

On the basis of SEM observations it was found that the width of the HAZ is not uniform and it is *ca.* 0.2 mm at the FZ face, but reaches 0.8 mm in the central area. In the HAZ, distinct differences in size and shape of the  $\gamma'$  precipitates can be observed. In the HAZ area, the primary  $\gamma'$  particles were subjected to a partial dissolving and repeated precipitation in the form of the secondary  $\gamma'$  phase. The secondary  $\gamma'$  precipitates were characterised by globular morphology and were much smaller than

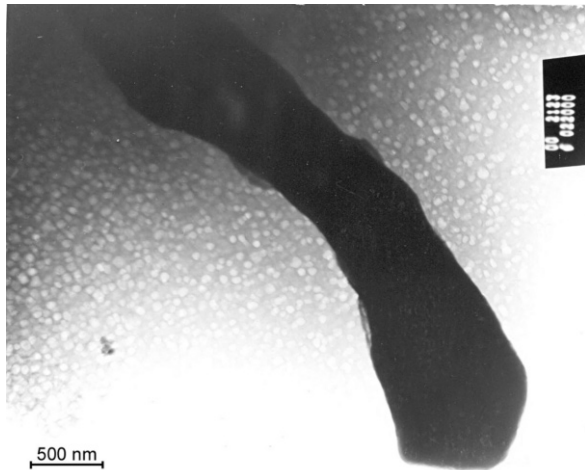


Fig. 8.  $M_{23}C_6$  carbide in the matrix of  $\gamma$  austenite and tiny precipitates of the  $\gamma'$  phase. TEM, bright field.

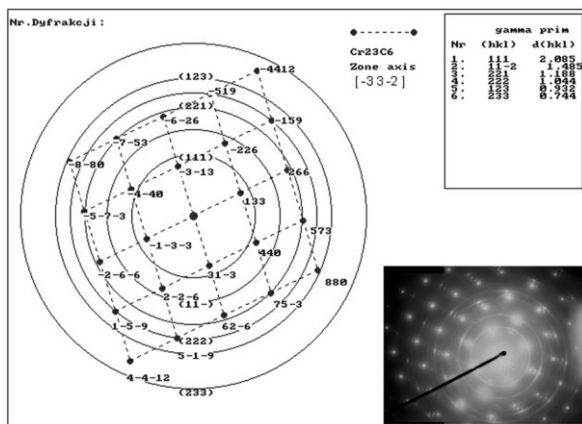


Fig. 9. The electron diffraction pattern from the area shown in Fig. 8 and its interpretation. The ring-shaped reflexes correspond to  $\gamma'$  phase; and the spot reflexes belong to an elementary cell of  $M_{23}C_6$  carbide.

the primary precipitates. Their estimated size was *ca.* 100 nm. The small sizes of the particles made it difficult to determine their exact dimensions.

The microstructure changes in the HAZ and FZ are shown in Fig. 10. A magnified picture of the boundary area in the base material and HAZ is shown in Fig. 11.

The single primary  $\gamma'$  precipitates resembling the arrangement of the RS carbides in FZ, identified in the HAZ, are of a particular interest. In addition,

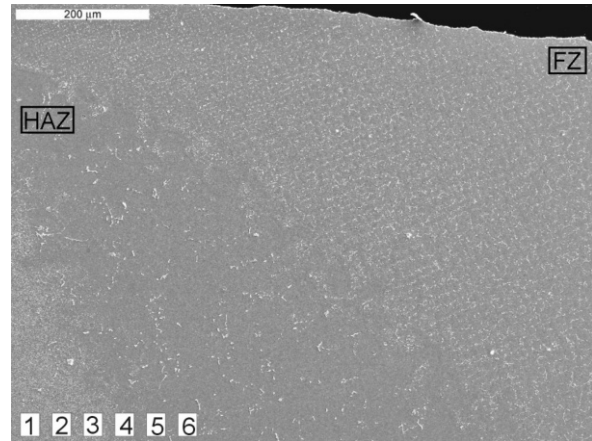


Fig. 10. The microstructure of the HAZ and the FZ. There is a visible morphology change of  $\gamma'$  phase and carbides. Etched with ML3, SEM, SE, 20 kV.

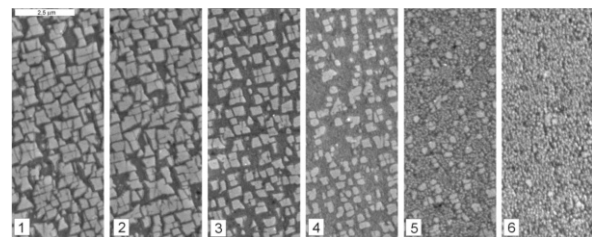


Fig. 11. Magnified areas in the interface between the base material and the HAZ, marked with figures from "1" to "6" in Fig. 10, reflecting change of  $Ni_3(AlTi)$  phase morphology. Etched with ML3, SEM, SE, 20 kV.

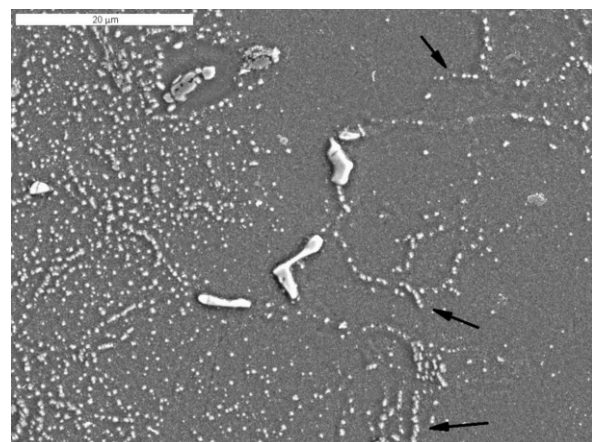


Fig. 12. Single primary  $\gamma'$  precipitates maintaining their morphological arrangement similar to those of carbides in the HAZ. Etched with ML3, SEM.

the  $\gamma'$  precipitates connect the carbides, forming distinct lines between them, indicated with the arrows in Fig. 12. These  $\gamma'$  precipitates probably contain more niobium and titanium, which partially substitute aluminium. The carbide-forming elements Nb and Ti are pushed away by the solidification front to interdendritic areas. At the proper carbon content, they create simple carbides (NbTi)C. If a local carbon concentration is too low or the cooling rate is too high, no carbide will be formed. Consequently, niobium and titanium will supersaturate the  $\gamma$  matrix and  $\gamma'$  phase. Such a supersaturated  $\gamma'$  phase created as the result of decomposition of (NbTi)C carbides was already identified in the 713C alloy [16]. The increased niobium content in the  $\gamma'$  phase raises its melting point. The  $\text{Ni}_3\text{Nb}$  stoichiometric phase dissolves at 1403 °C [35, 36]. Titanium reduces the melting point of  $\gamma'$ . The  $\text{Ni}_3\text{Ti}$  phase dissolves at 1378 °C. When titanium is added to an alloy, it is always present in  $\gamma'$  phase and is automatically included into the stoichiometric formula  $\text{Ni}_3(\text{AlTi})$ . Therefore, the influence of titanium on the melting point of  $\gamma'$  phase can be less intensive than that of niobium.

The differences in the melting points of the phases from the point of view of equilibrium systems at quasistatic heating and cooling are not significant. If the rapid heating is applied, the real differences can be far bigger.

This consideration explains the presence of the undissolved primary  $\gamma'$  phase in the interdendritic areas of the HAZ. Thus, the differences in the chemical composition of  $\gamma'$  phase can result in its higher hardness or its faster decomposition, melting and cracking in the HAZ.

Because of the small dimensions of  $\gamma'$  particles and slight differences in the chemical composition, it is difficult to confirm unmistakably such an effect of niobium on the basis of the metallographic examination. The abovementioned interpretation is partially confirmed by SEM observations in the FZ. In the interdendritic and intercellular areas, the formation of a carbide is preceded by increasing the concentration of niobium and titanium. On rapid cooling of the FZ, niobium is not completely bound in the NbC carbide and it supersaturates the matrix [16, 38]. The  $\gamma'$  phase supersaturated with niobium

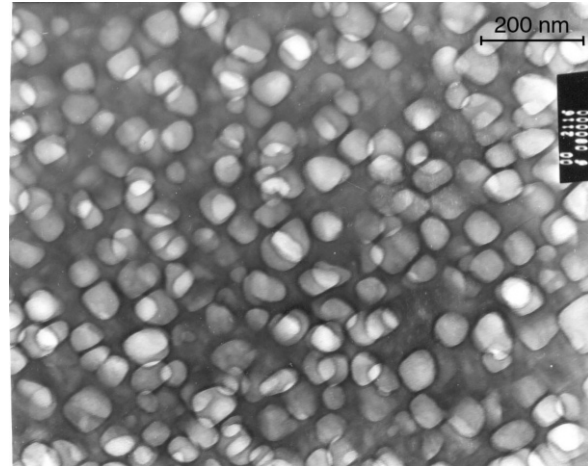


Fig. 13. The microstructure in the FZ made by TIG method. Granular  $\gamma'$  precipitates in  $\gamma$  austenite. TEM, bright field.

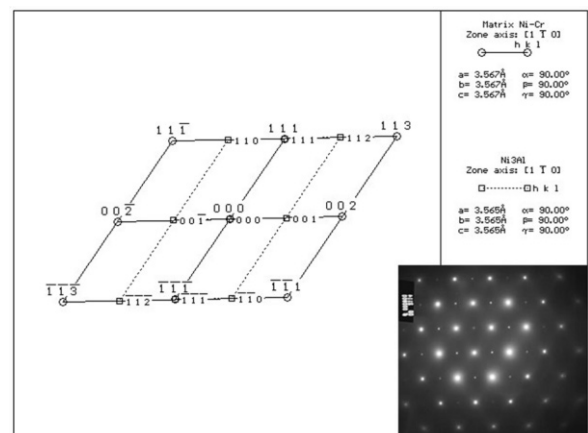


Fig. 14. The diffraction pattern of the area shown in Fig. 13 and its interpretation.

can precipitate together with the carbide from the supersaturated liquid pushed by the solidification front. This leads to blurring the interface carbide-matrix and, moreover, it can explain the presence of the developed eutectic mixtures  $\text{M}_x\text{C}_y-\gamma-\gamma'$ .

## 5.2. $\gamma'$ phase in the FZ

The TEM observations of the FZ revealed that the size of the secondary precipitates of  $\gamma'$  ( $\text{Ni}_3\text{Al}$ ) phase is 50 to 100 nm. These precipitates are 2 to 3 times larger than the  $\gamma'$  particles observed in the areas melted with the electron beam [26, 27]. This difference results from slower cooling of the FZ and

longer periods of time of the precipitation and coagulation of the  $\gamma'$  phase. In the FZ microstructure, no dislocations and stacking faults were observed, both on  $\gamma$ - $\gamma'$  interface and inside the  $\text{Ni}_3(\text{AlTi})$  precipitates. The precipitates in the FZ were observed in form of globules and parallelograms with rounded corners. Their quantity was evaluated as 70 %. This value corresponds to the quantity of the  $\gamma'$  phase in the base material. The microstructure of the FZ is shown in Fig. 13. On the basis of the electron diffraction patterns, one of which is shown in Fig. 14, it was found that the  $\gamma'$  precipitates are coherently coupled with the  $\gamma$  matrix according to the following crystallographic relationships:

$$\begin{aligned}(1\ 0\ 0)\text{Ni}_3\text{Al} &\parallel (1\ 0\ 0)_\gamma \\ (0\ 0\ 2)\text{Ni}_3\text{Al} &\parallel (0\ 0\ 2)_\gamma \\ (0\ 2\ 0)\text{Ni}_3\text{Al} &\parallel (0\ 2\ 0)_\gamma \\ (0\ 2\ 2)\text{Ni}_3\text{Al} &\parallel (0\ 2\ 2)_\gamma\end{aligned}$$

and

$$\begin{aligned}(1\ \bar{1}\ 0)\text{Ni}_3\text{Al} &\parallel (1\ \bar{1}\ 0)_\gamma \\ (1\ 1\ 3)\text{Ni}_3\text{Al} &\parallel (1\ 1\ 3)_\gamma \\ (1\ 1\ 1)\text{Ni}_3\text{Al} &\parallel (1\ 1\ 1)_\gamma \\ (0\ 0\ 2)\text{Ni}_3\text{Al} &\parallel (0\ 0\ 2)_\gamma\end{aligned}$$

No mismatch dislocations were found in the FZ, which proves a good coherence of the observed phases. On the basis of a few diffractograms taken at different locations using two electron microscopes, the lattice mismatch factor  $\Delta a/a = [(a\gamma' - a\gamma)/a\gamma]$  100 % was determined for the  $\gamma$  and  $\gamma'$  phases.

Its value ranges from +0.48 % to +0.71 %. The lattice parameter “a” of  $\gamma$  solution ranges from 3.5056 Å to 3.596 Å.

The lattice parameter of  $\gamma'$  [ $\text{Ni}_3(\text{AlTi})$ ] phase ranges from 3.5403 Å to 3.616 Å.

The value of the lattice mismatch factor is positive and close to the factors determined for the phases melted with the electron beam [26, 27]. The large positive mismatch factor points out that a large lattice deformation takes place around coherent  $\gamma'$  particles. A semi-coherent boundary can also be formed by the lattice deformation, because no mismatch dislocations were observed. No dislocations, which could be formed during the solidification of

the FZ as a result of thermal stresses, were evidenced.

The  $\gamma$  solid solution and a few coherent  $\gamma'$  particles precipitating at the initial stages of the FZ cooling do not significantly hinder the dislocation movement.

Therefore, the strain capacity of FZ during the cooling should be more feasible than that of HAZ and base material, at simultaneous increase in strengthening. In the FZ, after completed cooling and  $\gamma'$  precipitation processes, an increase in hardness up to  $439 \pm 10 \text{HV1}$  was observed. The hardness in the base material and in the HAZ was  $403 \pm 9 \text{HV1}$  and  $432 \pm 1 \text{HV1}$ , respectively. The increase of the strengthening was connected with dispersion of  $\gamma'$  particles, their good coherence and – indirectly – with the refinement of the RS carbides [39]. On the basis of the works [35, 36], it can be concluded that the semi-coherent  $\gamma'$  particles occur when the  $\Delta a/a$  factor is negative, and that they are accompanied by a dislocation network on the interface. The mismatch factor on the level of 0.7 % results in an increased strengthening and it corresponds to the Ni–Al–Nb alloys. However, higher  $\Delta a/a$  factors correspond to the  $\text{Ni}_3\text{Al}$  ( $\Delta a/a = 0.5\%$ ) and  $\text{Ni}_3\text{Ti}$  ( $\Delta a/a = 1.0\%$ ) phases. Taking into account these parameters, it can be presumed that the  $\gamma'$  phase with the approximate formula of  $\text{Ni}_3(\text{AlTiNb})$  should develop in the FZ.

## 6. Summary

1. In the FZ, hot cracks resulting from precipitation of  $\text{M}_{23}\text{C}_6$  or  $\text{M}_6\text{C}$  carbides based on chromium and molybdenum can occur. It is possible that the liquation cracks caused by the liquefied low-melting carbide phases could develop in the HAZ as well. These types of carbides are characterised by relatively low precipitation and decomposition temperatures, ranging between 760 °C and 1050 °C.
2. The cracks in the FZ can also be caused by the precipitation of eutectic mixtures of ( $\gamma$ - $\gamma'$ )- $\text{M}_x\text{C}_y$  type with very much diversified morphology, during solidification. On the FZ face surface, the  $\gamma$ - $\gamma'$  eutectic and com-

plex carbide phases were observed directly in the close proximity to each other. This proves that, in the matrix areas with non-homogeneous chemical composition, the  $\gamma$ - $\gamma'$  eutectic reaction can proceed at the temperature close to that of  $M_xC_y$  carbide precipitation. In addition, the presence of silicon can be conducive to lowering the melting point of that area by creating the low-melting NbSi compound. The NbC carbides and NbSi can create low-melting eutectics with the  $\gamma$  solid solution.

- Both in the FZ and in HAZ, small secondary precipitates of  $\gamma'$  [ $Ni_3(AlTi)$ ] phase, sized from 50 to 100 nm, were found. The mismatch factor of  $\gamma$  and  $\gamma'$  particles was positive, ranging from +0.48 % to +0.71 %, which is characteristic of the coherent precipitates of the  $Ni_3Al$  phase enriched with titanium and niobium. In the FZ microstructure, neither dislocations nor stacking faults were observed. In the HAZ microstructure, some primary, undissolved  $\gamma'$  precipitates, enriched with niobium that increases their melting point, were observed.

### Acknowledgements

The research was conducted as part of a programme – Fellowship, co-financed by European Union within European Social Fund and a research project of Wroclaw University of Technology No. 10010/I19.

### References

- HENDERSON M.B., ARRELL D., HEOBEL M., LARSON R., MARCHANT G., Nickel-Based Superalloy Welding Practices for Industrial Gas Turbine Applications, [www.msm.cam.ac.uk/phase-trans/2002/papers/APNickelWeldv2](http://www.msm.cam.ac.uk/phase-trans/2002/papers/APNickelWeldv2).
- RAMIREZ A.J., LIPPOLD J.C., *Mat. Sci. Eng. A*, 380 (2004), 245.
- RAMIREZ A.J., LIPPOLD J.C., *Mat. Sci. Eng. A*, 380 (2004), 259.
- QIAN M., LIPPOLD J.C., *Acta Mater.*, 51 (2003), 3351.
- HARO S., RAMIREZ C., MENDOZA E., RODRIGUEZ R., COLAS R., *Mater. Charact.*, 51 (2003), 22.
- PODREZ-RADZISZEWSKA M., JÓZWIK P., *Arch. Civil Mech. Eng.*, 4 (2011), vol. 11, 1011.
- EZUGWU E.O., WANG Z.M., MACHADO A.R., *Mater. Process Tech.*, 86 (1999), 1.
- YANG F.M., SUN X.F., ZHANG W., KANG Y.P., GUAN H.R., HU Z.Q., *Mater. Letters*, 49 (2001), 160.
- ASM Handbooks On-line <http://products.asminternational.org/hbk/index.jsp>.
- YIN F.S., SUN X.F., LI J.G., GUAN H.R., HU Z.Q., *Scripta Mater.*, 48 (2003), 425.
- BERTHOLD P., ARAND L., VEBERT C., MICHON S., *Computer Coupling of Phase Diagrams and Thermochemistry*, 28 (2004), 159.
- PHADESHIA H.K.D.H., *Nickel Based Superalloy*, [www.msm.cam.ac.uk/phase-trans/2003/superalloys/superalloys.html](http://www.msm.cam.ac.uk/phase-trans/2003/superalloys/superalloys.html).
- SUN W.R., LEE J.H., SEO S.M., CHEO S.J., HU Z.Q., *Mat. Sci. Eng. A*, 271 (1999), 143.
- CHEN J., LEE J.H., JO C.Y., CHEO S.J., LEE Y.T., *Mat. Sci. Eng. A*, 247 (1998), 113.
- JIANG W.H., YAO X.D., GUAN H.R., HU Z.Q., *Metall. Mater. Trans.*, 30A (1999), 513.
- LACHOWICZ M., DUDZIŃSKI W., *Archiv. Metall. Mater.*, 1 vol. 55 (2010), 305–315.
- CHEN W., CHATURVEDI M.C., RICHARDS N.L., MCMAHONG., *Metall. Mater. Trans.*, 29A (1998), 1947.
- QIAN M., LIPPOLD J.C., *Weld J.*, 6 (2003), 145.
- CHEN W., CHATURVEDI M.C., RICHARDS N.L., *Metall. Mater. Trans.*, 32A (2001), 931.
- HUAXIN L., JONES R.H., *Mat. Sci. Eng. A*, 192/193 (1995), 563.
- HUAXIN L., CHAKI T.K., *Mat. Sci. Eng. A*, 192/193 (1995), 570.
- OJO O.A., RICHARDS N.L., CHATURVEDI M.C., *Scripta Mater.*, 51 (2004), 683.
- OJO O.A., CHATURVEDI M.C., *Mat. Sci. Eng. A*, 403 (2005), 77.
- OJO O.A., RICHARDS N.L., CHATURVEDI M.C., *Scripta Mater.*, 50 (2004), 641.
- OJO O.A., RICHARDS N.L., CHATURVEDI M.C., *Scripta Mater.*, 51 (2004), 683.
- LACHOWICZ M., DUDZIŃSKI W., HAIMANN K., PODREZ-RADZISZEWSKA M., *Mat. Sci. Eng. A*, 479 (2008), 269.
- LACHOWICZ M., DUDZIŃSKI W., PODREZ-RADZISZEWSKA M., *Mater. Charact.*, 59 (2008), 560.
- LACHOWICZ M., ZEMAN M., *Przegląd Spawalnictwa*, 8 (2007), 22.
- DEEVI S.C., SIKKA V.K., *Intermetallics*, 4 (1996), 357.
- DEEVI S.C., SIKKA V.K., LIU C.T., *Prog. Mater. Sci.*, 42 (1997), 177.
- LIU C.T., STRINGER J., MUNDY J.N., HORTON L.L., ANGELINI P., *Intermetallics*, 5 (1997), 579.
- PEARSON W.B., *A handbook of lattice spacings and structures of metals and alloys, vol. 2*, Pergamon Press, (1967), 79.
- MUKHERJI D., GILLES R., BARBIER B., GENOVESE D., DEL, HASSE B., STRUNZ P., WRÓBLEWSKI T., FUESS H., RÖSLER J., *Scripta Mater.*, 48 (2003), 333.
- MAEBASHI T., DOI M., *Mat. Sci. Eng. A*, 373 (2004), 372.
- HANSEN M., *Constitution of binary alloys*, McGraw-Hill Book Company INC; (1958), 118.

- [36] CZYRSKA-FILEMONOWICZ A., *The influence of helium on the structure of nickel-base alloys. Papers of commission of metallurgy and foundry*, Polish Academy of Sciences (1989), 32.
- [37] LOOMIS W.T, FREEMAN J.W, SPONSELLER D.L., *Met. Trans.*, 3 (1972), 989.
- [38] LACHOWICZ M., *Archiv. Found Eng.*, 3, vol. 10, (2010), 11.
- [39] SOMOZA A., SANTOS G., GES A., VERSACI R., PLAZAOLA F., *Phys. Stat. Sol.*, 174 (1999), 189.

*Received 2010-10-08*

*Accepted 2012-06-25*